International Journal on Advances in Intelligent Systems, vol 14 no 1 & 2, year 2021, http://www.iariajournals.org/intelligent_systems/

Towards Frictional 3D Object Shape Scanning and Reconstruction by Means of Vibrissa-like Tactile Sensors

Lukas Merker
Department of Mechanical Engineering
Technische Universität Ilmenau, Germany
e-mail: lukas.merker@tu-ilmenau.de

Abstract—**Interacting with the environment, mobile robots could benefit from advanced tactile sensors complementing optical sensors, consequently gathering overlapping information. In the animal kingdom, there are numerous examples of tactile sensors just as the vibrissae of rats. These tactile hairs enable the animals, inter alia, to detect object shapes based on few contacts. Vibrissae themselves consist of dead tissue and, thus, all sensing is performed in the support of each vibrissa. This characteristic and simple measuring structure provides an inspirational framework for developing tactile sensor concepts. Within the present paper, we take advantage of a recently developed mechanical model of a vibrissa-inspired sensor for 3D object shape scanning and reconstruction. It consists of a cylindrical, one-sided clamped bending rod, which is swept along a 3D object surface undergoing large deflections. Instead of assuming an ideal contact (no frictional effects) as in previous publications, the contact model includes Coulomb's friction. Simulating frictional scanning sweeps, the focus is on both generating the support reactions (observables) at the base of the rod theoretically and subsequently using these quantities in order to reconstruct a sequence of contact points approximating the scanned object surface. Our investigation reveals that (of course) the generated support reactions are affected by friction, but (surprisingly) the reconstruction error seems to be largely invariant against friction.**

Keywords–Vibrissa; tactile sensor; surface sensing; surface reconstruction.

I. INTRODUCTION

Object shape detection and obstacle avoidance are key topics in mobile robotics [1][2]. In nature, almost all species solve these tasks by sensing overlapping information of the environment, e.g., combining information provided by the sense of vision and touch. However, in mobile robotics, the majority of data is frequently gathered solely relying on optical (vision) sensors – the NASA Rover Perseverance[1] of the 2020 Mars mission serves as a striking example. In some cases, completely dispensing with tactile sensing carries the risk of missing information under poor visibility and impedes the interaction with environmental objects. Therefore, advanced tactile sensors hold great potential to complement optical sensors. Developing tactile sensors, engineers often draw their inspiration from biology. Besides the human skin, another prominent and particularly well-researched tactile sense organ are the mystacial vibrissae in the snout region of the rat. Based on few contacts with an object of interest, these tactile hairs allow for the detection of the object's distance, orientation, shape and texture [3]–[5]. Moreover, vibrissae are used for sensing fluid flows [6].

Basically, a vibrissa consists of a long and slender hair-shaft with no receptors along its length, which is conically and pre-curved shaped [7][8] and supported by the Follicle Sinus Complex (FSC) [9][10]. Making contact with an object of interest, mechanical stimuli are transmitted through the hair-shaft to the FSC, where the actual sensing is realized by a wide variety of mechanoreceptors. Despite the fact that it is not conclusively clarified how exactly animals manage to determine object features, e.g., object shapes [11], the remarkable structure of natural vibrissae has frequently been transferred into technical sensor concepts over the last decades. A variety of these approaches pursue the goal of scanning and reconstructing object shapes. Basically, these approaches all share a common structure: a slender, more or less flexible probe, mimicking the vibrissal hair-shaft, one-sided attached to some kind of measuring device, representing the FSC. Besides this basic structure, approaches differ considerably in modeling the probe and its support, as well as in the evaluated signals (observables) and the procedure of localizing contact points in space. For the process of object scanning, two different approaches have been established in literature [12]:

- *The tapping strategy*: The object is scanned by repeatedly pushing the probe against various points of the object. In doing so, the artificial vibrissa is retracted from the object right after the very first contact (small pushing angles). Consequently, the deformations of the probe remain small and a linear bending theory is sufficient to accomplish the localization of the contact point [13]–[16] based on measurements of the curvature or torque [16], angles and/or moments [13]–[15] at the support of the probe.
- *The sweeping strategy*: For object scanning, the probe is pushed against an object far beyond the very first contact, consequently undergoing large deformations and sliding over the objects surface [12][17]. Therefore, a highly flexible and elastic probe is mandatory.

The latter strategy is a particularly promising approach due to its passive feasibility [12], e.g., using the robot movement as an actuation without the need of repeatedly making and releasing contact. Moreover, due to the high flexibility of the used probe, the sensor design offers high collision robustness. Passing an object, the probe bends out of way, consequently sweeping along the object and continuously transducing signals to the measuring unit, see Figure 1. Due to these advantages, we focus on the sweeping strategy, which has received less attention in the literature than the tapping one [12].

---

[1] https://mars.nasa.gov/mars2020/spacecraft/rover/cameras/, June 09,2021

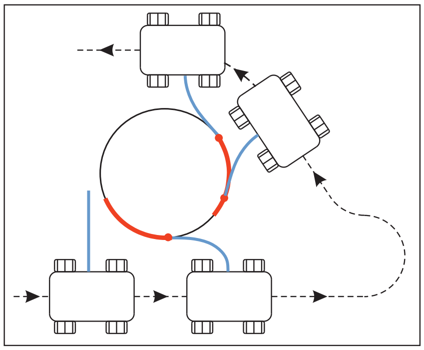

Figure 1. Schematic application example of a rover exploring a circular object adapted from [20].

In [18], the authors used a steel probe attached to a six axis hub load cell to measure the support reactions (three forces and three moments) at the base of the probe. The whole assembly was swept along several edged 3D objects while measuring the support reactions. During scanning, lateral slip of the artificial vibrissa was prevented by actively adjusting the scanning direction w.r.t. the surface normal, which was continuously determined exploiting the measured support reactions. An initial-value problem based on a non-linear bending theory was used to determine the contact position in space. Finally, the authors successfully reconstructed a cloud of contact points and, thus, provided a proof of concept. A similar approach was used in [17] considering the process of object scanning and reconstruction as a plane problem and focusing on an analytical treatment. The presented sensor concept consists of a one-sided clamped probe, which is swept along a 2D object contour. Just as in [18], the sensing concept is based on the support reactions, i.e., two forces and one moment at the clamping of the probe. By analogy with [18], the deformation of the probe is described using an arc-length parameterization of the rod axis and using non-linear Euler-Bernoulli bending theory to express its curvature. However, the major difference compared to [18] is that the problem is sub-divided into two (inverse) steps, which are both treated fully analytically and validated using an experimental setup:

- *Step 1*: simulating scanning sweeps in order to generate the support reactions (observables) at the base of the rod theoretically, assuming the object contour to be known, and
- *Step 2*: using the generated support reactions from the previous step in order to reconstruct a sequence of contact points, finally approximating the original object contour.

In contrast, [18] used a numerical approach and limited the consideration to Step 2.

In [12], a sweeping-based reconstruction algorithm was presented, which is based on repeatedly inferring from one contact point to the next one by continuous measurement of the moment and rotation angle at the base of the probe. This method dispenses the need of force measurements, but it is limited to tangential contacts along the probe and is not suitable for 3D reconstruction.

In [19], the authors modeled an artificial vibrissa using a multi-body system. There, the step of generating the support reactions in 3D space was included, but only for a preset (a priori known) impressed force. In addition, this force was restricted to be always perpendicular to the probe tangent at the contact point. Finally, focusing on the design of the probe considering pre-curved and tapered shapes, the reconstruction process was realized based on a neural network - in this way, unique mappings between the input and output signals are proven but without any analytical correlations.

Summarizing the mentioned approaches, the focus is frequently on the reconstruction of the contact point location in space based on different measured signals at the support of the probe (Step 2). Thus, a theoretical generation of the support reactions (Step 1) is rarely taken into account. However, including the latter process into consideration holds great potential to gain insights into the scanning process and to provide a simulation tool, allowing for parameter studies to investigate the sensor system without having to rely on a large number of experiments. For instance, the theoretical generation of support reactions allows us to provide a data basis for different predefined (well-known) friction parameters. In practice, such parameters are mostly unknown and hard to predefine. Therefore, following [17] and [1], we focus on both mentioned Steps 1 and 2. Our investigation differs from previous works in using the sweeping scanning strategy for 3D object reconstruction passively, i.e., without actively adjusting the scanning direction w.r.t. surface normals of the object [18]. Moreover, as far as the authors know, it is the first work to consider frictional effects in that context. To date, it is an open question how friction affects the 3D reconstruction result when using the sweeping scanning strategy. For instance, imagining two objects of the same shape made of different materials, it is unclear if different friction pairings (probe/object) might erroneously lead to different shape estimations.

In contrast to [18], our investigations are not limited to edged 3D objects. Instead, objects with wide-ranging curvature are scanned in the presence of lateral slip. The presented model differs from [19] in considering a reaction force resulting from the sweep of a rod along a mathematically described object surface instead of a preset impressed force. Unlike [12], our reconstruction method is suitable for 3D object shapes. Moreover, it is not limited to tangential contacts, but also includes tip contacts between the probe and the object. Finally, we present a novel approach to approximate the micromechanics of the contact during object scanning based on Coulomb's law of friction, which distinguishes the present paper from similar works.

The remainder of the paper at hand is structured as follows: In Section II, we present the mechanical model of the vibrissa-inspired sensor for 3D shape scanning and reconstruction, starting with the basic setup in Section II-A. In Section II-B, we focus on the contact mechanics during object scanning assuming Coulomb friction. After some preliminary geometrical considerations, we derive the deformation equations of the probe. Then, following the procedure of [17], we separately analyze the above-mentioned Steps 1 and 2, respectively. In Section III, we firstly demonstrate the general appearance of the simulated scanning sweeps. Subsequently, the simulation results of Steps 1 and 2 are analyzed with the overall goal of clarifying the influence of the friction coefficient on both, the support reactions at the base of the probe and the reconstruction error. Finally, the results of the present paper are summed up and some future research subjects are identified in Section IV.

II. MODELLING

Within this section, we build up and mathematically describe the mechanical model of the vibrissa-like tactile sensor concept step by step, starting with the basic setup.

A. *Basic setup*

The mechanical model consists of two interacting components in a fixed Cartesian coordinate system (x, y, z) (global frame), see Figure 2:

1. a highly flexible probe, one-sided clamped at it's lower end ("foot", "base") with constraint direction $\vec{e}_z$;
2. a fixed 3D target object.

The probe is modeled as a circular cylindrical rod with an originally straight axial line. Its shape is characterized by the length L and a constant circular cross-section, resulting in a constant second moment of area I. Guided by the biological paragon vibrissa, the cross-sectional dimensions of the rod are extremely low compared to its length. Moreover, we assume the rod to consist of a homogeneous and isotropic, linear elastic Hooke's material. Based on these assumptions, the mechanical behavior of the rod is essentially determined by a constant Young's modulus E resulting in a constant bending stiffness EI. From the outset, we introduce the following units of measure in order to allow any kind of scaling [17]:

$$\begin{aligned} [length] &:= L, \\ [force] &:= \frac{EI}{L^2}, \\ [moment] &:= \frac{EI}{L}. \end{aligned} \tag{1}$$

Remark 1. *We point out that, e.g., $[lenght] := L$ denotes that all lengths are measured in the unit and value of L.*

The object is assumed as a rigid body with a strictly convex, smooth surface $z = C(x, y)$. Within the present paper, we consider the example of an elliptic paraboloid

$$(x, y) \mapsto C(x, y) = a\,x^2 + b\,y^2 + h, \tag{2}$$

with $a, b > 0$ and $h \in (0, 1)$ and unit normal vector

$$\vec{n}(x, y) = \frac{1}{\sqrt{4a^2x^2 + 4b^2y^2 + 1}} \begin{pmatrix} -2ax \\ -2by \\ 1 \end{pmatrix} \tag{3}$$

The scanning sweep of the rod along the object's surface is realized by a kinematic drive, i.e., the clamping position $P_0(x_0, y_0, 0)$ of the rod (system input) is shifted incrementally along a straight trail in the x-y-plane. This process is considered quasi-statically. Interacting with the object, the rod gets bent in the inference of some unknown contact force $\vec{f}$ forming an elastic line in $\mathbb{R}^3$. In doing so, the strict convexity of the object ensures, that there is always only one contact point $P_1(\xi, \eta, \theta)$ between the rod and the object [21], see Figure 2.

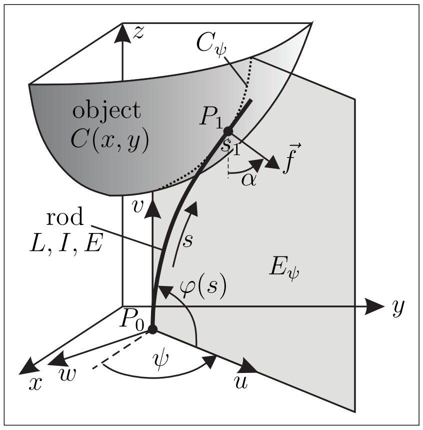

Figure 2. Mechanical model for object shape scanning and reconstruction rod in contact with an object's surface adapted from [1].

B. *3D frictional contact model*

It was concluded in [20], that (based on the assumptions in Section II-A) the elastic line of the rod shrinks to one in some deformation plane E_ψ with (yet) unknown orientation ψ, see Figure 2. However, this plane bending working hypothesis was made assuming an ideal contact, i.e., in the absence of friction. Here, we now analyze the problem using a more realistic approach, roughly approximating the micro-mechanics of the contact using Coulomb's law of friction [22]. Therefore, we assume the constraining force $\vec{f}$, transmitted through the object contact as composed of two components, see Figure 3:

$$\vec{f} = \vec{f}_n + \vec{f}_t \tag{4}$$

The component $\vec{f}_n$ is aligned with the outer normal vector $\vec{n}_1$ of the surface C at P_1.

$$\vec{f}_n = |\vec{f}_n| \cdot \vec{n}_1, \tag{5}$$

In contrast, lying in the tangent plane at P_1 of C, the component $\vec{f}_t$ still has an unknown orientation. Both components are coupled by Coulomb's law of friction:

$$\vec{f}_t = -\mu |\vec{f}_n| \frac{\vec{v}}{|\vec{v}|}, \tag{6}$$

where $\mu = \frac{|\vec{f}_t|}{|\vec{f}_n|} = \tan(\zeta)$ is the coefficient of friction with friction angle ζ and $\vec{v}$ is the sliding velocity. Being restricted to a quasi-static model, we cannot make any statements about the sliding velocity $\vec{v}$. However, according to (6), the tangential force solely depends on the direction of sliding but not on the actual speed of sliding. Therefore, the basic idea within the present paper is to interpret a sequence of contact points $(P_{1,i})_{i\in\mathbb{N}}$ as the trajectory of P_1 on C, see Figure 3. Then, the direction opposing the sliding velocity at some point $P_{1,k}$ is approximated using the previous contact point $P_{1,k-1}$ in the following way:

$$\vec{f}_t^* = |\vec{f}_t^*| \cdot \vec{t}^*, \quad \text{with} \quad \vec{t}^* = \frac{P_{1,k-1} - P_{1,k}}{|P_{1,k-1} - P_{1,k}|} \tag{7}$$

The distance $P_{1,k-1} - P_{1,k}$ of two successive contact points decreases with decreasing step size of the system input and, thus, using tiny incremental steps, (7) approaches a tangent vector of C at $P_{1,k}$, pointing from $P_{1,k}$ to $P_{1,k-1}$.

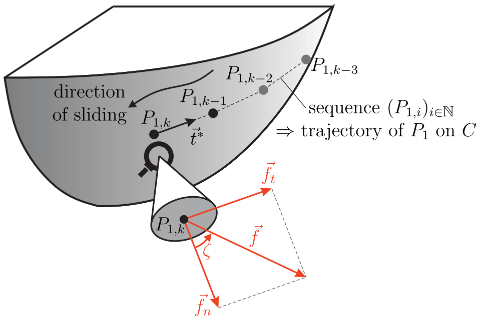

Figure 3. Sequence of contact points between rod and object, representing the trajectory of P_1 on C with the constraining force at $P_{1,k}$ (see enlarged section).

C. Preliminary geometrical considerations

Figure 4 shows the constraining force $\vec{f}$ acting at P_1 for both friction partners, i.e., for the object's surface in Figure 4(a) and for the bending rod in Figure 4(b). As can be seen from Figure 4(b), all forces are considered to act at the center of the rod's cross-section for sake of simplicity and, thus, their lines of action intersect the axial line of the rod. Otherwise, the contact forces might create moments about the axial line, possibly causing twist deformations, which are neglected in our theory. This simplification is justified by the extremely small cross-sectional dimensions of the rod under consideration (and the natural paragon vibrissa).

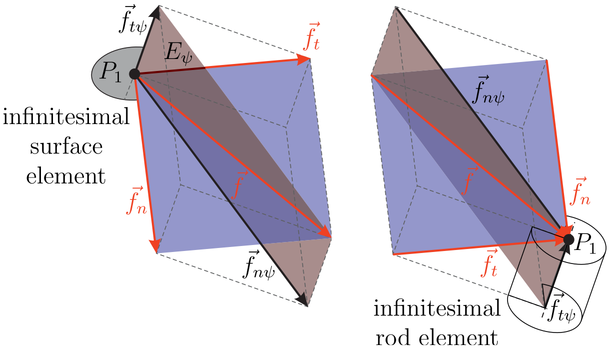

(a) (b)

Figure 4. Components of the constraining force $\vec{f}$ at P_1: (a) infinitesimal surface element; (b) infinitesimal rod element.

Dropping twist deformations of the rod, Figure 2 and Figure 4 clarify the following geometrical relationships: The constraining force $\vec{f}$ defines the deformation plane E_ψ in such a way that the geometrical condition $\{P_0, P_1, \vec{e}_z, \vec{f}\} \in E_\psi$ is fulfilled [20]. Introducing the local coordinate system (u,v,w) (local frame), see Figure 2, we come up with the following transformation rules [20]:

$$\begin{pmatrix} \vec{e}_u \\ \vec{e}_v \\ \vec{e}_w \end{pmatrix} = \mathbf{T}(\psi) \cdot \begin{pmatrix} \vec{e}_x \\ \vec{e}_y \\ \vec{e}_z \end{pmatrix}, \qquad \begin{pmatrix} \vec{e}_x \\ \vec{e}_y \\ \vec{e}_z \end{pmatrix} = \mathbf{T}^{-1}(\psi) \cdot \begin{pmatrix} \vec{e}_u \\ \vec{e}_v \\ \vec{e}_w \end{pmatrix} \tag{8}$$

$$\text{with} \qquad \mathbf{T}(\psi) = \begin{pmatrix} \cos(\psi) & \sin(\psi) & 0 \\ 0 & 0 & 1 \\ \sin(\psi) & -\cos(\psi) & 0 \end{pmatrix} \tag{9}$$

In the following, all considerations are restricted to the plane E_ψ (u-v-plane). This plane intersects the surface C in some intersection curve $C_\psi = E_\psi \cap C$, see Figure 2. The tangent and normal directions

$$\vec{t}_\psi = \vec{e}_w \times \vec{n}_1 \qquad \vec{n}_\psi = \vec{t}_{1\psi} \times \vec{e}_w \tag{10}$$

of C_ψ at P_1 are used to split the constraining force $\vec{f}$ into two orthogonal components $\vec{f}_{n\psi}, \vec{f}_{t\psi} \in E_\psi$, see Figure 4. The relation $\vec{f} = \vec{f}_n + \vec{f}_t = \vec{f}_{n\psi} + \vec{f}_{t\psi}$ is visualized by means of a rectangular cuboid in Figure 4. There, the purple diagonal plane is spanned by $\vec{f}_n$ and $\vec{f}_t$, the brown diagonal plane, namely E_ψ, is spanned by $\vec{f}_{n\psi}$ and $\vec{f}_{t\psi}$ and the line of intersection of these planes denotes the resulting force $\vec{f}$.

D. The plane elastic line

The analysis within this section is largely analog with [20] and therefore roughly outlined here. Within the deformation plane E_ψ (u-v-plane), the elastic line of the rod is described parameterizing the axis of the rod by means of its slope angle φ in dependence on its natural coordinate arc length s. Moreover, using Euler's constitutive law $\kappa(s) = m(s)$ in dimensionless representation (mind (1)) we finally end up in a system of Ordinary Differential Equations (ODEs) [20]:

$$\boxed{\begin{array}{ll} u'(s) = \cos(\varphi(s)) & \varphi'(s) = \kappa(s) \\ v'(s) = \sin(\varphi(s)) & \kappa'(s) = f\cos(\varphi(s) - \alpha) \end{array}} \tag{11}$$

In (11), f is the magnitude of $\vec{f}$ and α is defined as the signed angle between $\vec{f}$ and $-\vec{e}_v$, see Figure 2:

$$\alpha = \operatorname{atan2}(\vec{e}_u \cdot \vec{f}, -\vec{e}_v \cdot \vec{f}) \tag{12}$$

The ODE system (11) describes the plane elastic line of the rod. Depending on the corresponding problem, Boundary Conditions (BCs) or Initial Conditions (ICs) are to be adjoint in Section II-E and II-F, respectively.

E. Step 1: Generating the support reactions theoretically

The preliminary process of theoretically generating the support reactions at each particular clamping position P_0 reflects/replaces the actual experiment of sweeping the rod along the object while measuring the support reactions (observables). For Step 1, we assume

- the object surface C,
- the clamping position P_0,
- and the friction coefficient μ

to be known (preset) in advance. In this way, Step 1 is used as a valuable tool allowing for the generation of the support reactions during scanning sweeps with different preset friction coefficients.

Following [1] and [20], we distinguish two different contact phases, see Figure 5:

- For tip contacts, the position of contact along the rod $s_1 = 1$ is known, but the angle $\varphi_1 = \varphi(1) > \tilde{\alpha}$ is unknown.
- In contrast, for tangential contacts, the position of contact along the rod s_1 is unknown, but instead, we have the angular relationship $\varphi = \tilde{\alpha}$.

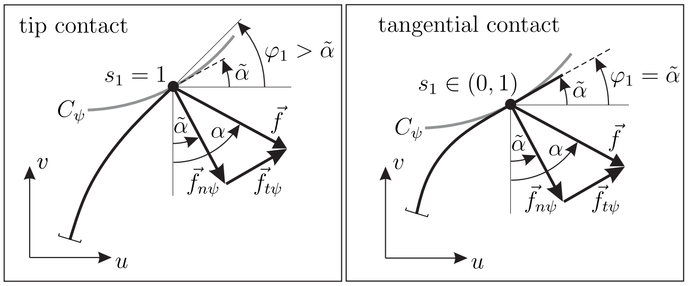

Figure 5. Comparison between tip and tangential contact with angular relationships within the deformation plane E_ψ.

Inspired by Figure 5, we define the angle $\tilde{\alpha}$ as the tangent slope angle of C_ψ at P_1:

$$\tilde{\alpha} = \operatorname{atan2}(\vec{e}_u \cdot \vec{n}_\psi, -\vec{e}_v \cdot \vec{n}_\psi) \tag{13}$$

Consequently, we find the following BCs for tip (14) and tangential contacts (15), respectively:

$$\boxed{\begin{array}{ll} u(0) = 0 & u(1) = u_1 \\ v(0) = 0 & v(1) = v_1 \\ \varphi(0) = \dfrac{\pi}{2} & \\ & \kappa(1) = 0 \end{array}} \tag{14}$$

$$\boxed{\begin{array}{ll} u(0) = 0 & u(s_1) = u_1 \\ v(0) = 0 & v(s_1) = v_1 \\ \varphi(0) = \dfrac{\pi}{2} & \varphi(s_1) = \tilde{\alpha} \\ & \kappa(s_1) = 0 \end{array}} \tag{15}$$

In (14) and (15), u_1 and v_1 are the coordinates of P_1 w.r.t. the local frame. Finding equilibrium states of the rod in contact with the object is achieved using a Matlab algorithm. Basically, the algorithm repeatedly solves the Boundary-Value Problems (BVPs) (11)&(14) and (11)&(15) for each clamping position using shooting methods to determine the unknown parameters s_1, $|\vec{f}_n|$, u_1 and ψ.

Remark 2. *More specifically, assuming reasonable starting values for these unknown parameters, the used algorithm proceeds using* (2)–(15) *in the following way:*
For each clamping position P_0*...*

(a) *... determine*
  - *the orientation of the local frame using* (8)*,*
  - *the contact point* P_1 *evaluating* (2) *and* (8)*,*
  - *the coordinate* v_1 *using* (8)*,*
  - *the normal force* $\vec{f}_n$ *using* (3) *and* (5)*,*
  - *the tangential force* $\vec{f}_t$ *using* (6) *and* (7) *,*
  - *the resulting force* $\vec{f}$ *based on* (4)*,*
  - *the components* $\vec{f}_{n\psi}$ *and* $\vec{f}_{t\psi}$ *of* $\vec{f}$ *using* (10)*,*
  - *the angles* α *and* $\tilde{\alpha}$ *using* (12) *and* (13)*.*

(b) *... try to find a solution for the BVPs* (11)&(14) *or* (11)&(15)*, respectively.*

(c) *... repeat A and B varying the parameters* s_1, $|\vec{f}_n|$, u_1 *and* ψ *until an equilibrium state has been found.*

Once all relevant parameters are known, the support reactions

$$f_{0u} = -f\sin(\alpha), \qquad f_{0v} = -f\cos(\alpha) \tag{16}$$

$$m_{0w} = f[u_1\cos(\alpha) + v_1\sin(\alpha)] \tag{17}$$

are calculated and expressed w.r.t. the global frame using (8):

$$\vec{m}_0 = m_{0x}\vec{e}_x + m_{0y}\vec{e}_y + m_{0z}\vec{e}_z \tag{18}$$

$$\vec{f}_0 = f_{0x}\vec{e}_x + f_{0y}\vec{e}_y + f_{0z}\vec{e}_z \tag{19}$$

Finally, this procedure results in a sequence of support reactions for an entire scanning sweep, starting from the very first contact between the rod and the object and terminating with the detachment of the rod.

F. Step 2: Reconstructing contact points

The process of reconstructing a sequence of contact points in space based on the support reactions of Section II-E reflects the actual sensor application. Of course, the shape of the object, as well as the friction coefficient, are unknown in this context. Instead, only the following quantities are assumed to be known in advance:

- the support reactions (18)&(19) generated in Step 1 (or measured using a real experiment)
- the clamping position P_0

However, compared to Step 1, the mechanical problem of Step 2 is relatively simple, as the orientation of the deformation plane E_ψ is directly evident evaluating

$$\psi = -\operatorname{atan2}(m_{0x}, m_{0y}) \tag{20}$$

Then, expressing (18)&(19) w.r.t. the local frame using (8), f and α follow from (17)

$$f = \sqrt{f_{0u}^2 + f_{0v}^2}, \quad \alpha = -\operatorname{atan2}(f_{0u}, f_{0v}) \tag{21}$$

and the curvature at P_0 writes

$$\kappa(0) = -m_{0w} \tag{22}$$

Using (22), we have the following ICs:

$$\boxed{\begin{array}{l} u(0) = 0 \\ v(0) = 0 \\ \varphi(0) = \dfrac{\pi}{2} \\ \kappa(0) = -m_{0w} \end{array}} \tag{23}$$

In contrast to Step 1, including a BVP, Step 2 is characterized by the IVP (11)&(23), which can be solved without shooting methods. Instead, it is integrated numerically using an event function, which cancels further computation if the termination condition $\kappa(s_1) = 0$ is fulfilled. This condition results from the single contact point scenario due to the modeling assumptions, in contrast to [21]. Then, the last step of the numerical integration includes the solutions for s_1, u_1, v_1 and φ_1, see Figure 5. Finally, the contact position in space is expressed with respect to the global frame using (8).

III. RESULTS & DISCUSSION

The following results are based on simulated scanning sweeps of the probe along a 3D object, which are illustrated in Section III-A. We analyze the theoretically generated support reactions at the base of the probe in Section III-B. In Section III-C, these support reactions are used to reconstruct sequences of contact points.

A. *Simulated scanning sweeps*

Within the present paper we use (2) with the parameters $a = 0.5$, $b = 1$ and $h = 0.4$ as an exemplary object surface. The geometry parameters are chosen based on preliminary studies. On the one hand, $a \neq b$ ensures, that the results are not restricted to surfaces of revolution. On the other hand, the chosen object distance h ensures the occurrence of both tip and tangential contacts. The scanning trail is assumed to be parallel to the x-axis. The clamping position $P_0(x_0, y_0, 0)$ of the rod is displaced along this trail decreasing the system input x_0 with constant y_0. In doing so, we simulated scanning sweeps for $y_0 = -0.4 : 0.2 : +0.4$ and $\mu = 0 : 0.1 : 0.4$ resulting in a total number of 25 scanning sweeps, of which four exemplary sweeps are shown in Figure 6. There, the scanning sweeps are represented by sequences of elastic lines (equilibrium states), where tip contacts are colored in blue and tangential ones in red for $s \in (0, s_1)$ and black for $s \in (s_1, 1)$. For reasons of clarity, only one in ten calculated deformation states is shown in Figure 6. Essentially, a scanning sweep may exhibit two fundamentally different characteristics, see Figure 6:

- For the special case $y_0 = 0$, the scanning trail entirely lies within a symmetry plane of the object (x-z-plane). Regardless of the friction coefficient, this arrangement results in a special case of an entirely plane scanning sweep, see Figure 6(a) ($\mu = 0$) and Figure 6(b) ($\mu = 0.4$). Such a plane scanning sweep always terminates with a “snap-off” (dynamical detachment) of the deformed rod from the object [23]. It is to be noted, that increasing friction coefficients result in slightly delayed “snap-offs” and, thus, increase the scanning range, compare Figures 6(a) and 6(b).
- For the more general case $y_0 \neq 0$, a completely different scanning behavior is observed: As seen in Figure 6(c) ($y_0 = 0.2$, $\mu = 0$) and Figure 6(d) ($y_0 = 0.2$, $\mu = 0.4$) the rod bends around the object and finally smoothly detaches from the object stress-free, i.e., without any snap-off. In general, for the case $\mu = 0$, the symmetry of the object w.r.t. y-z-plane results in a symmetric appearance of the elastic lines, see Figure 6(c). This symmetry is not maintained with increasing mu, see Figure 6(d). Instead, the orientation of the bending plane E_ψ in Figure 6(d) seems to lack behind the one in Figure 6(c) as a consequence of the frictional force.

Remark 3. *The reason for showing Figure 6 at the very beginning of this section is to create a figurative idea about the scanning process. However, it is important to highlight that Figure 6 actually results at the very end of the simulation process after performing Steps 1 and 2.*

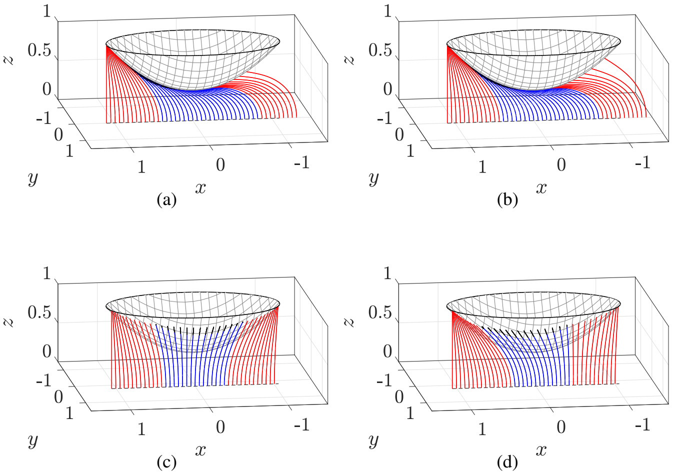

Figure 6. Exemplary scanning sweeps in negative x-direction represented by sequences of elastic lines: (a) $y_0 = 0$, $\mu = 0$; (b) $y_0 = 0$, $\mu = 0.4$; (c) $y_0 = 0.2$, $\mu = 0$; (d) $y_0 = 0.2$, $\mu = 0.4$.

B. *Step 1: Generating the support reactions*

Figures 7 and 8 show the components of the support reactions (18) and (19) resulting from ten exemplary scanning sweeps plotted against the system input x_0 in dependence on different friction coefficients μ. In both figures, the phase transitions from tip to tangential contact and vise versa are marked with an ’o’. Note that Figures 7 and 8 are to be read from right to left due to the scanning direction (negative x-direction). Figure 7 represents the plane special case ($y_0 = 0$) identified in Section III-A and, thus, the dark blue ($\mu = 0$) and yellow curves result from the scanning sweeps in Figures 6(a) and 6(b). Regardless of the friction coefficient, the components f_{0y}, m_{0x} and m_{0z} are zero during the entire scanning sweep and therefore obscure each other for different values of μ. This fact confirms the observation that for $y_0 = 0$ all scanning sweeps entirely take place in the x-z-plane. It is striking that the remaining components of the support reactions are affected by the friction coefficient, e.g., the component f_{0z} consistently increases with increasing μ. Moreover, comparing the values x_0 at the end of each scanning sweep (left side of each curve), confirms that an increasing coefficient results in a longer overall contact phase. It can be seen that the phase transitions are characterized by discontinuities (kinks). However, the friction coefficient seems to have little impact on these discontinuities and the location of the phase transitions in general.

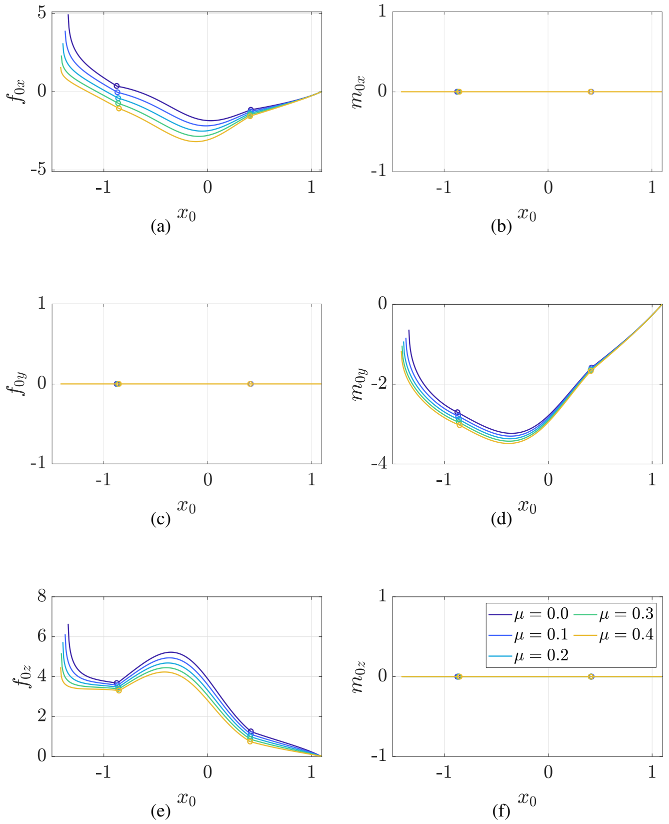

Figure 7. Components of the support reactions (observables) $\vec{f}_0$ and $\vec{m}_0$ resulting from simulated scanning sweeps with $y_0 = 0$ plotted against the system input x_0 in dependence on different preset friction coefficients μ.

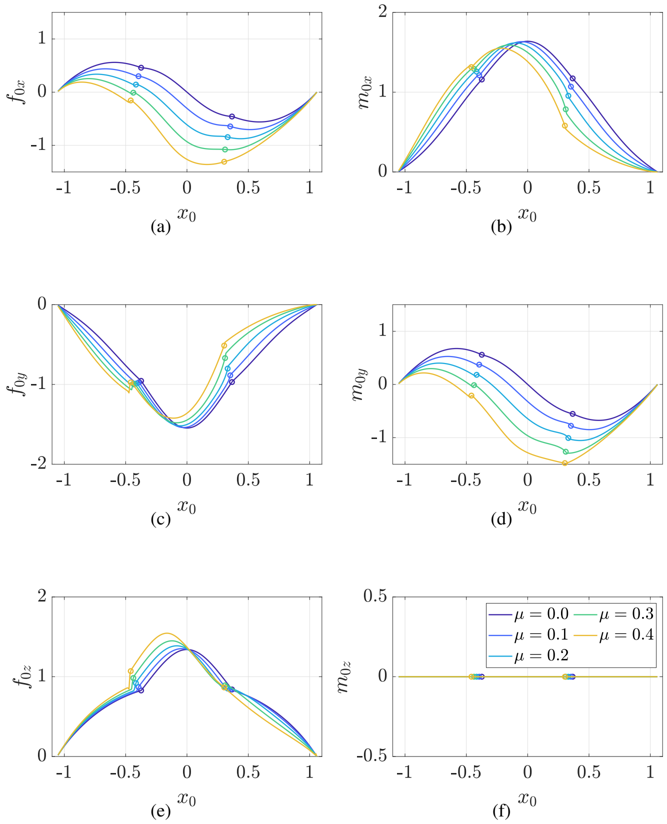

Figure 8. Components of the support reactions (observables) $\vec{f}_0$ and $\vec{m}_0$ resulting from simulated scanning sweeps with $y_0 = 0.2$ plotted against the system input x_0 in dependence on different preset friction coefficients μ.

Exemplary considering the case $y_0 = 0.2$, Figure 8 represents the more general case $y_0 \neq 0$ of a scanning sweep, see Section III-A. Again, the dark blue ($\mu = 0$) and yellow curves correspond to the scanning sweeps in Figures 6(a) and 6(b), respectively. In contrast to Figure 7, only the component m_{0z} is zero during the entire scanning sweep due to the plane bending assumption (ignoring twist deformation), see Section II-C. The remaining components are strongly affected by the friction coefficient. The dark blue curves ($\mu = 0$) are vertical or point symmetric as a consequence of the object's symmetry. For increasing friction coefficients, the maximum values of the support reactions are increasingly shifted in the negative direction of x_0. However, for $y_0 \neq 0.2$, the friction coefficient has no impact on the position of the rod detachment. Moreover, all support reactions fall to zero at the end of the scanning sweep. This confirms the stress-free detachment of the rod from the object. Finally, compared to Figure 7, the phase transitions seem to be stronger affected by the friction coefficient. For instance, an increasing friction coefficient results in delayed phase transitions and causes discontinuities (small jumps). These jumps might result from a sudden change of the sliding trajectory (and, thus, the direction of the frictional force), when the contact point s_1, which is one in case of tip contact, suddenly begins to move along the rod axis in case of tangential contact.

Summarizing, the support reactions are strongly affected by the friction coefficient. Unfortunately, Figures 7 and 8 do not yet allow us to draw further conclusions about the object's shape. Therefore, we consider Step 2 in the next section.

C. Step 2: Reconstructing contact points

Figure 9 shows 25 sequences of Reconstructed Contact Points (RCPs) based on the generated support reactions of 25 simulated scanning sweeps. The isometric view in Figure 9(a) shows the original object surface C alongside with the RCPs. Moreover, a top view with hidden object surface is given in Figure 9(b). In contrast to Figure 6, where only one in ten calculated deformation states is displayed, the point sequences in Figure 9 include the RCP of each single simulation step. Consequently, each sequence of RCPs rather appears as a line than a multitude of points. The high density of RCPs ensures a good approximation of the tangent direction in (7). Considering Figure 9 it becomes clear that the sequences of RCPs depend on both the scanning trail position y_0 and the friction coefficient μ. Mind: for each scanning trail $y_0 = -0.4 : 0.2 : +0.4$, five scanning sweeps with different friction coefficients $\mu = 0 : 0.1 : 0.4$ were simulated. This results in a bundle of five sequences of RCPs for each y_0, marked in Figure 9(b). For instance, considering Figure 9(b), scanning the object on the red scanning trail ($y_0 = +0.2$) results in five sequences of RCPs (circled in red), depending on the friction coefficient, see color legend in Figure 9(a). For reasons of clarity, only one scanning trail is shown in Figure 9(b), while the others are simply pointed out giving the corresponding values of y_0 (gray).

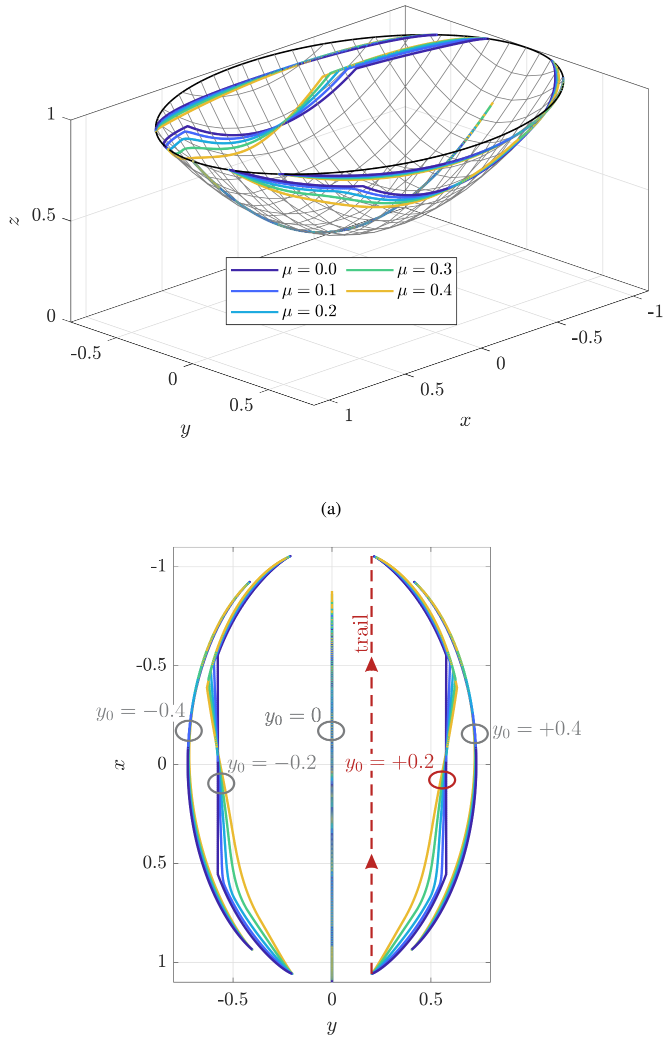

(a)

(b)

Figure 9. Reconstructed sequences of contact points based on 25 simulated scanning sweeps: (a) original object surface superimposed with reconstructed contact points in dependence on the friction coefficient μ; (b) top view including information about the scanning trails.

Considering Figure 9, the following results must be highlighted:

- For $y = 0$ it appears that the sequences of RCPs coincide to a large extend regardless of the friction coefficient. However, this does not mean that the RCPs are not affected by friction. Instead, for increasing friction coefficients, the RCPs shift along the object's surface within the x-z-plane. For instance, it can be seen that for the largest friction coefficient $\mu = 0.4$, the sequence of RCPs exceeds all others. This reflects the fact that (for the plane special case) increasing friction coefficients increase the scanning range due to a delayed "snap-off".
- For $y \neq 0$, the sequences of RCPs do no longer coincide for different friction coefficients. While outermost sequences ($|y_0| = 0.4$) differ slightly for different friction coefficients, the inner ones ($|y_0| = 0.2$) seem to be stronger affected by friction. In this way, the sequences of RCPs based on simulations with $\mu = 0$, are completely symmetric w.r.t. y-z-plane. In contrast, for $\mu > 0$ the frictional force causes asymmetries. For the preset object distance $h = 0.4$, scanning sweeps with $|y_0| = 0.4$ do not include tangential contacts in contrast to those with $|y_0| = 0.2$. This statement remains true regardless of the friction coefficient. For $|y_0| = 0.2$, the transitions between tip and tangential contacts and vise versa are clearly identifiable by the discontinuities (kinks) of the sequences of RCPs. For instance, considering the dark blue sequence ($\mu = 0$, $y_0 = 0.2$), the first discontinuity (at $x \approx 0.5$) reflects the transition from tip to tangential contact and the second one (at $x \approx 0.5$) the inverse transition, see Figure 6(a). Increasing friction coefficients weaken the extent of the first discontinuity and reinforce the extent of the second one, see Figure 9(b).

Summarizing, increasing friction coefficients affect the sequences of RCPs. This may falsely give the impression, that increasing friction results in increased distortion of the reconstruction result. For instance, in Figure 9(b), the reconstruction result appears to be distorted in a way that the width of the object in y-direction is underrated at the beginning and overrated at the end of the scanning sweep. This seems to be the case especially with the yellow sequences ($\mu = 0.4$). However, it is important to understand that such distortion does not take place at all. Instead, the isometric view in Figure 9(a) suggests that all reconstructed points lie perfectly on the original object surface. To highlight and verify this suspicion, the reconstruction error of each RCP is calculated and shown by the color-bar in Figure 10. The reconstruction error is defined as the smallest (perpendicular) distance between a RCP P_{rek} and the original object surface C: Let $P(a, b, c) \in C$ be the point of C closest to P_{rek}. Then $\vec{e} = \overrightarrow{PP_{rek}}$ is collinear with $\vec{n}(a, b)$ and the error of P_{rek} is $|\vec{e}|$. Obviously, the maximum reconstruction error lies within the numerical boundaries regardless of the friction coefficient. This fact confirms an empirical observation and hypothesis originally made in [20] and leads to the final result of the present paper:

- For each clamping position P_0 during scanning, the frictional force affects the deformation of the rod and, thus, the contact point P_1 on C.
- Consequently, the support reactions at the base of the rod are affected by friction
- Evaluating the support reactions in order to reconstruct the contact position in space, different friction coefficients would result in different locations of the RCP. For instance, a point P_1^*, which is reconstructed in the presence of friction ($\mu > 0$) is different from the point P_1, which would have been reconstructed in the absence of friction

- However, both points P_1^* and P_1 would lie on the original object surface C.
- Thus, friction leads (of course) to a shift of the RCPs on the scanned 3D object surface itself, but does not affect the reconstruction error. This is what we refer to as friction invariant reconstruction.

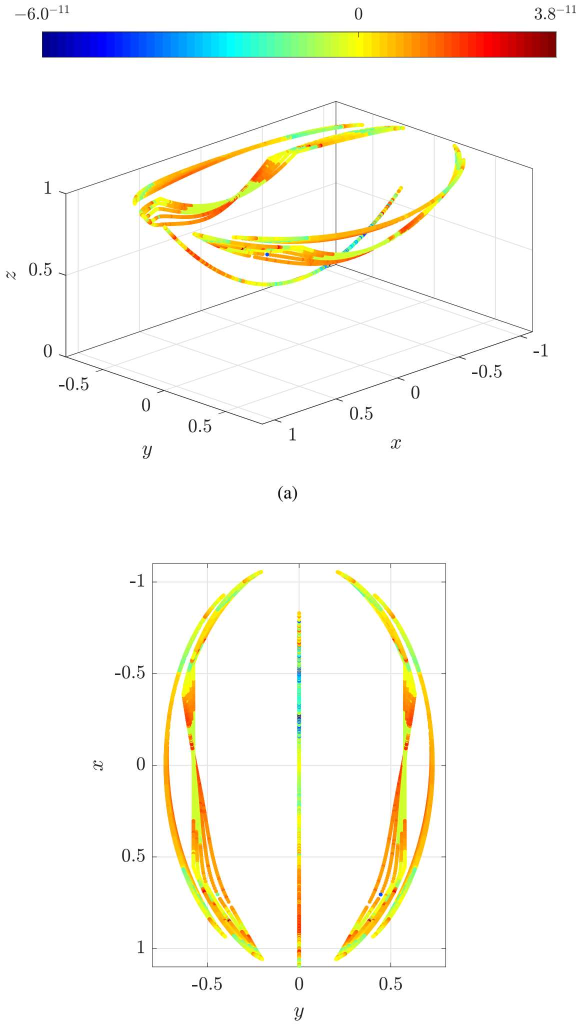

(a)

(b)

Figure 10. Reconstructed sequences of contact points based on 25 simulated scanning sweeps highlighting the reconstruction error using a color-bar: (a) isometric view; (b) top view.

IV. CONCLUSION

Within this paper, we presented a vibrissa-inspired tactile sensor concept for 3D object surface scanning and reconstruction. For that purpose, a one-sided clamped rod was swept along the object's surface by incremental displacements of its clamping position, relatively to the object. In contrast to other publications, we firstly approximated the micro-mechanics of the contact assuming Coulomb friction, instead of presuming an ideal contact (no frictional effects). Being restricted to a quasi-static model, the direction of the frictional force was approximated inferring from one contact point to the next one. Based on the novel modeling approach, two consecutive processes were analyzed separately: Firstly, scanning sweeps along a known object surface were simulated with a preset friction coefficient in Step 1. In this way, the support reactions (observables) at the base (clamping) of the rod were generated theoretically. Secondly, we demonstrated how to use the support reactions from Step 1 in order to reconstruct sequences of contact points, finally approximating the surface of the scanned object. Both steps were implemented in a Matlab algorithm and simulated to demonstrate the general applicability. The simulation results showed that friction (obviously) affects the support reactions during object scanning. However, using these support reactions to reconstruct contact points, it surprisingly turned out that the reconstruction result is friction invariant, i.e., friction does not affect the reconstruction error. This is a novel and not self-evident finding, revealing a major advantage of the vibrissa-inspired sensor concept. Thus, extending the mechanical model including Coulomb friction yields new insights compared to previous works. Instead of representing a self-contained investigation, the present paper should be seen as a preliminary concept study, indicating that the presented measuring principle is highly suited to complement optical sensors in the environmental exploration of robots. In doing so, we aim to implement the presented concept into an intelligent tactile sensor in the future.

Finally, it remains to mention that the results and hypotheses of the present paper are based on a quasi-static model. This means the scanning sweep is realized by incremental displacements of the clamping, resulting in a sequence of consecutive equilibrium states. Against this backdrop, only static friction but no dynamical effects, e.g., stick-slip effects can be discussed. However, instead of repeatedly stopping the clamping position in order to wait for the stationary state, in practice, the scanning sweep rather has to be thought of as a continuous movement of the clamping and, thus, a continuous sweep of the rod over the object surface. Therefore, dynamical effects like stick-slip effects as observed in [20] are likely to occur in reality. Therefore, it remains to verify the theoretical results on practical examples by using an experimental setup, which has already been attacked in the first steps.

REFERENCES

[1] L. Merker, M. Scharff, K. Zimmermann, and C. Behn, "Surface Sensing of 3D Objects Using Vibrissa-like Intelligent Tactile Sensors," INTELLI 2020, The Ninth International Conference on Intelligent Systems and Applications, Porto, Portugal, October 18–22, 2020, pp. 18–23. ISBN: 978-1-61208-798-6.

[2] J. Minguez, F. Lamiraux, and J. Laumond, "Motion planning and Obstacle Avoidance," In: Springer Handbook of Robotics. Ed. by B. Siciliano; O. Khatib, Berlin, Heidelberg: Springer, pp. 1177–1202, 2016.

[3] M. Brecht, B. Preilowski, and M. M. Merzenich, "Functional architecture of the mystacial vibrissae," Behav. Brain Res., vol. 84, pp. 81–97, 1997.

[4] E. Guić-Robles, C. Valdivieso, and G. Guajardo, "Rats can learn a roughness discrimination using only their vibrissal system," Behav. Brain Res., vol. 31, pp. 285–289, 1989.

[5] G. E. Carvell and D. J. Simons, "Biometric Analyses of Vibrissal Tactile Discrimination in the Rat," J. Neurosci., vol. 10, pp. 2638–2648, 1990.

[6] T. J. Prescott, B. Mitchinson, and R. A. Grant, "Vibrissal behavior and function," Scholarpedia, vol. 6, p. 6642, 2011.

[7] H. M. Belli, A. E. T. Yang, C. S. Bresee, and M. J. Z. Hartmann, “Variations in vibrissal geometry across the rat mystacial pad: Base diameter, medulla, and taper,” J. Neurophysiol., vol. 117, pp. 1807–1820, 2016.

[8] D. Voges et al., “Structural Characterization of the Whisker System of the Rat,” IEEE Sens. J., vol. 12, pp. 332–229, 2012.

[9] D. Campagner, M. H. Evans, M. S. E. Loft, and R. S. Petersen, “What the whiskers tell the brain,” Neurosci. vol. 368, pp. 95–108, 2018.

[10] S. Ebara, T. Furuta, and K. Kumamoto, “Vibrissal mechanoreceptors,” Scholarpedia, vol. 12, p. 32372, 2017.

[11] J. H. Solomon and M. J. Z. Hartmann, “Radial distance determination in the rat vibrissal system and the effects of Weber’s law,” Phil. Trans. R. Soc. B., vol. 366, pp. 3049–3057, 2011.

[12] J. H. Solomon and M. J. Z. Hartmann, “Extracting object contours with the sweep of a robotic whisker using torque information,” Int. J. Robot Res. vol. 29, pp. 1233–1245, 2010.

[13] J. H. Solomon and M. J. Z. Hartmann, “Artificial whiskers suitable for array implementation: accounting for lateral slip and surface friction,” IEEE Trans. Robot., vol. 24, pp. 1157–1167, 2008.

[14] D. Kim and R. Möller, “Biomimetic whiskers for shape recognition,” Proceedings of the 1995 IEEE International Conference on Robotics and Automation, Nagoya, Japan, 21-27 May 1995, pp. 1113–1119.

[15] M. Kaneko, N. Kanayama, and T. Tsuji, “Active antenna for contact sensing,” IEEE Trans. Robot. Autom., vol. 14, pp. 278–291, 1998.

[16] A. E. Schultz, J. H. Solomon, M. A. Peshkin, and M. J. Z. Hartmann, “Multifunctional Whisker Arrays for Distance Detection, Terrain Mapping, and Object Feature Extraction,” IEEE International Conference on Robotics and Automation, Barcelona, Spain, 18-22 April 2005, pp. 2588–2593.

[17] C. Will, C. Behn, and J. Steigenberger, “Object contour scanning using elastically supported technical vibrissae,” ZAMM J. Appl. Math. Mec., vol. 98, pp. 289–305, 2018.

[18] T. N. Clements and C. D. Rahn, “Three-Dimensional Contact Imaging With an Actuated Whisker,” IEEE Trans. Rob., vol. 22, pp. 844–848, 2006.

[19] L. A. Huet, J. W. Rudnicki, and M. J. Z. Hartmann, “Tactile sensing with whiskers of various shapes: determining the three-dimensional location of object contact Based on mechanical signals at the whisker base.” Soft Robot., vol. 4, pp. 88–103, 2017.

[20] L. Merker, J. Steigenberger, R. Marangoni, and C. Behn, “A vibrissa-inspired highly flexible tactile sensor: scanning 3D object surfaces providing tactile images,” Sensors, vol. 21, 2021. DOI: 10.3390/s21051572.

[21] L. Merker, S. J. Fischer Calderon, M. Scharff, J. H. Alencastre Miranda, and C. Behn, “Effects of Multi-Point Contacts during Object Contour Scanning Using a Biologically-Inspired Tactile Sensor,” Sensors, vol. 20, 2020. DOI: 10.3390/s20072077.

[22] V. L. Popov, “Contact mechanics and friction,” Springer, 2010.

[23] L. Merker, M. Scharff, and C. Behn, “Approach to the dynamical scanning of object contours using tactile sensors,” IEEE International Conference on Mechatronics (ICM), pp. 364–369, 2019. DOI: 10.1109/ICMECH.2019.8722882.